Journal of Materials Science & Technology 119 (2022) 1–10

Contents lists available at ScienceDirect

Journal of Materials Science & Technology

journal homepage: www.elsevier.com/locate/jmst

Research Article

# Static spheroidization and its effect on superplasticity of fine lamellae in nugget of a friction stir welded Ti-6Al-4V joint

C.L. Jia[a,b], L.H. Wu[a,c,*], P. Xue[a,c], H. Zhang[a,c], D.R. Ni[a], B.L. Xiao[a], Z.Y. Ma[a]

[a] Shi-Changxu Innovation Center for Advanced Materials, Institute of Metal Research, Chinese Academy of Sciences, Shenyang 110016, China
[b] School of Materials Science and Engineering, University of Science and Technology of China, Shenyang 110016, China
[c] Key Laboratory of Nuclear Materials and Safety Assessment, Institute of Metal Research, Chinese Academy of Sciences, Shenyang 110016, China

ARTICLE INFO

*Article history:*
Received 24 August 2021
Revised 3 October 2021
Accepted 13 October 2021
Available online 24 February 2022

*Keywords:*
Friction stir welding
Titanium alloys
Spheroidization mechanism
Coalescence
Superplasticity
Static annealing

ABSTRACT

The spheroidization of the lamellar structure can greatly contribute to the superplasticity of the nugget zone (NZ) of Ti alloy welds, which is the key to achieve the integral superplastic forming of welds for the fabrication of large-scale complex components. However, the spheroidization process is complex and costly since it cannot be obtained generally, unless the lamellae suffers from a large deformation. In this study, the static spheroidization was achieved for the fine lamellae structure in the nugget of a friction stir welded (FSW) Ti-6Al-4V joint, particularly by the annealing without any deformation. The special $\alpha/\beta$ interface obeying a Burgers orientation relationship (BOR) after FSW was first time directly observed, whose effect on the spheroidization was discussed. A new static spheroidization mechanism with the gradual coalescence of the adjacent lamellae was discovered, which we named as "termination coalescence". There was a slower coarsening rate in the lamellar structure than in the classical equiaxed one, due to the BOR in the lamellae, although both of them exhibited a volume diffusion character during annealing. Consequently, the similar superplasticity can be achieved for the base material and NZ after annealing. This study can provide a new way to the spheroidization and a theoretical basis for the integral superplastic forming of welds during production.



## 1. Introduction

Superplastic forming (SPF) has been widely used to fabricate the complex components of titanium (Ti) alloys in the manufacturing industry, due to its near-net forming, and weight reduction etc [1,2]. It is necessary to combine the SPF and welding for the large-scale Ti alloy components, as the internal structure is becoming more complex and larger at present. Great attentions have been drawn to fabricate the monolithic Ti alloy components via the integral SPF of the large size welded sheets in recent years.

The precondition for the integral SPF of the entire joint is to achieve the similar superplastic deformation ability in the weld zone and the base material (BM). Generally, the good superplastic property exhibits in the rolled BM sheet of Ti alloy with a fine-grained microstructure. However, the coarse lamellar structure in the welds can largely destroy the superplastic property of the Ti alloy sheet after fusion welding. Thus, the fusion welds are not suitable for the integral SPF so far [3,4].

Alternatively, friction stir welding (FSW) as a solid-state joining has been originally designed to treat the low-melting material-aluminum alloys [5], but recently applied for high-melting metals, such as Ti alloys [6–10]. A fine-grained microstructure can be achieved in the nugget zone (NZ) generally, due to the severe deformation and dynamic recrystallization during FSW. Therefore, the FSW shows a great potential to achieve the excellent superplastic deformation abilities as the BM.

It was reported that the key zone influencing the superplasticity of the entire joints was the nugget zone (NZ), and in most FSW parameters, a fine fully lamellar microstructure was obtained in the NZ [11,12]. Our previous studies indicated that the fine fully lamellae could get excellent superplasticity, however, the superplastic abilities of the lamellae in the NZ was still less than that of the mill-annealed structure in the BM [13]. The static spheroidization of lamellae before deformation was recognized as the critical reason for the excellent superplasticity of lamellae [14]. Therefore, it is very necessary further to investigate the spheroidization process of the fine lamellae in the NZ during FSW.

* Corresponding author at: Shi-Changxu Innovation Center for Advanced Materials, Institute of Metal Research, Chinese Academy of Sciences, Shenyang 110016, China.
*E-mail address:* lhwu@imr.ac.cn (L.H. Wu).

https://doi.org/10.1016/j.jmst.2021.10.054
1005-0302/

Much progress has been made to elucidate the spheroidization mechanism of $\alpha$ plates in both theoretic and experimental way over the past years [15–17], due to the excellent mechanical properties of spheroidized structure, such as strength–ductility synergy, and superior fatigue behavior [18]. Generally, the spheroidization process could be divided into dynamic spheroidization and static spheroidization, which generally occurred during hot deformation and static annealing, respectively. During the dynamic spheroidization process, the substructures are normally generated inside the lamellar structure under the applied stress, and then the lamellae were fragmented by the formation and deepening of grooves in the presence of various surface tension at the interphase/intraphase triple junctions [18,19].

In static spheroidization, the termination migration as a static spheroidization modal generally occurred during static annealing [20]. However, the lamellar structure cannot be easily spheroidized under static annealing, due mainly to the existence of the Burgers orientation relationship (BOR) in the $\alpha/\beta$ interface. There was the very low interface energy in the $\alpha/\beta$ interface with the BOR hard to be broken. Mostly, the static spheroidization of lamellae was completed with the assistance of prestrain to break the BOR [18,20,21]. The prestrain can break the $\alpha/\beta$ interface with the BOR, as well as bring the different kinds of substructures into the lamellar structure. The static spheroidization occurred under the driven force of the curvature difference for the lamellae at the static annealing, due to the edge recession and the thickness coarsening of lamellae [22]. Therefore, the deformation has been an indispensable process for both the static and dynamic spheroidization of lamellae in Ti alloys.

However, some reports demonstrated that without the assistance of deformation, the lamellae was still spheroidized for the fine lamellae that obtained by the FSW Ti-6Al-4V alloy, where the spheroidization fraction was improved from 2.2% to 20.8% after static annealing at 800 °C for 5 min [13,23]. The spheroidization phenomenon was totally different from the commonly-accepted spheroidization model. Therefore, it is of great significance to delve the static spheroidization of this fine lamellar microstructure in terms of the scientific and engineering aspects. The phenomenon can be benefit to enrich the spheroidization theory from the scientific aspect. From the engineering aspect, to further explore the static spheroidization of the fine and low-aspect ratio lamellae is in favour of a better superplasticity for the NZ. The rapid spheroidization of lamellae without deformation can also provide a promising way to simplify the processing in the industrial production.

In the study, a fully lamellar microstructure in the NZ was prepared by FSW. Both the lamellae in the NZ and the equiaxed structure in the BM were held for the different time before superplastic tension, aiming (a) to explore the static spheroidization mechanism of fine lamellae in the NZ without the assistance of deformation; (b) to investigate the difference of the microstructure evolution for the lamellar structure in the NZ and the classical equiaxed structure in the BM; (c) to evaluate the feasibility for the similar superplasticity of the BM and NZ via the static annealing.

## 2. Experimental methods and procedures

The as-received materials were the mill-annealed 2 mm Ti–6Al–4V alloy sheets. A friction stir welding was performed on the Ti-6Al-4V sheets at a travel speed of 150 mm/min and a rotation rate of 500 rpm (500–150). A W-25Re welding tool was used with the shoulder of 11 mm in diameter. Argon gas was also used to prevent the oxidation of the joint surface during welding.

The microstructure was then characterized by an optical microscopy (OM, MEF4A), transmission electron microscopy (TEM, FEI, Tecnai $G^2$ 20), scanning electron microscopy (SEM, Supra 55), and electron backscatter diffraction (EBSD, HKL Channel 5). The specimens for the OM, SEM and EBSD were all ground to 2000 grits with SiC papers, and then polished with the $SiO_2$ solution. Kroll's reagent was used to etch the OM and SEM specimens. The EBSD and TEM specimens were prepared by the twin-jet polishing with a chemical solution of 6 mL $HClO_4$ + 34 mL $CH_3OH$ + 60 mL $C_4H_9OH$ at −25 °C.

The reference directions were simplified in the work as follows: WD, the welding direction; ND, the normal direction; TD, the transverse direction; RD, the rolling direction of the BM, and the welding direction (WD) of the specimens by FSW. The advancing side and the retreating side were simplified as the AS and the RS, respectively. The dogbone-shaped tensile specimens with the gage length of 2.5 mm were cut from the NZ and the BM, respectively. The long axis for the specimens was parallel to the TD of the Ti alloy sheets. Prior to the test, the high-temperature coating was performed on the specimens to prevent the oxidation during annealing and tensile test process. The specimens were heated at 10 °C/min, and then were held at the annealing temperature of 900 °C for 5, 20, 60, 180, and 300 min. A previous study indicated that a fully lamellar structure achieved the excellent superplasticity at 900 °C [13], which was the main reason for the selection of annealing temperature in this study. The superplastic tensile specimens were also tested under the strain rate of $1 \times 10^{-3}$ $s^{-1}$ at 900 °C. More than 300 lamellae (or grains) were measured to calculate the average thickness and aspect ratio of the lamellae.

## 3. Results and discussion

### 3.1. Microstructure of the BM and NZ

Fig. 1(a) shows the typical cross-sectional morphology of the Ti-6Al-4V friction stir welded joints. There is no defect in the welded joint with the NZ similar to "basin shape". The narrow gray zone between the NZ and BM presented to be the thermo-mechanically affect zone (TMAZ) and the heat affected zone (HAZ). The NZ and BM became the main influencing zones on the superplasticity of the entire welded joint, due to the narrow TMAZ and HAZ resulted from the low thermo-conductivity of Ti-6Al-4V material, similar to the previous study [12].

Fig. 1(b–e) shows the OM and TEM micrographs of the BM and NZ. The mill-annealed microstructure consisted of equiaxed $\alpha$ (white contrast in Fig. 1(b)) and $\beta$ phase (black contrast in Fig. 1(b)), together with most subgrains in the BM (Fig. 1(d)). The fine fully lamellar microstructure was observed in the NZ after FSW (Fig. 1(c, e)), indicating that the welding temperature has exceeded the $\beta$ phase transus temperature.

The grain size of the primary $\beta$ phase ($\beta_p$) was approximately 15 $\mu$m (Fig. 1(c)). There were very few dislocations in the lamellar microstructure. The thickness and aspect ratio of the lamellae were 180 ± 70 nm and 7. 71 ± 3.75, respectively. The lamellar structure that obtained by FSW was much finer than the conventional one obtained by fusion welding and annealing from the $\beta$ single phase field .

The high resolution and Fourier transformation in Fig. 2 showed that the the directions of the two phase for the electron beams were parallel, that was $[2\bar{1}\bar{1}0]_\alpha // [11\bar{1}]_\beta$. The direction of $[2\bar{1}\bar{1}0]$ for the $\alpha$ phase was also parallel to that of $[11\bar{1}]$ for the $\beta$ phase, and the corresponding base plane $(0002)_\alpha$ for the HCP was parallel to the $(101)_\beta$ plane for the BCC. Thus, the orientation relationship of the lamellar $\alpha$ and $\beta$ phase can be determined with $\{0001\}_\alpha // \{110\}_\beta$, and $<11\bar{2}0>_\alpha // <111>_\beta$, indicating the classical BOR in Ti alloys [24]. Thus, the $\alpha/\beta$ phase boundaries in this study followed the BOR with the low-energy $\alpha/\beta$ interface.

To our best knowledge, it is the first time to experimentally verify the BOR of the lamellar $\alpha/\beta$ interface in the FSW joint. Although some researchers inferred that there existed the BOR be-

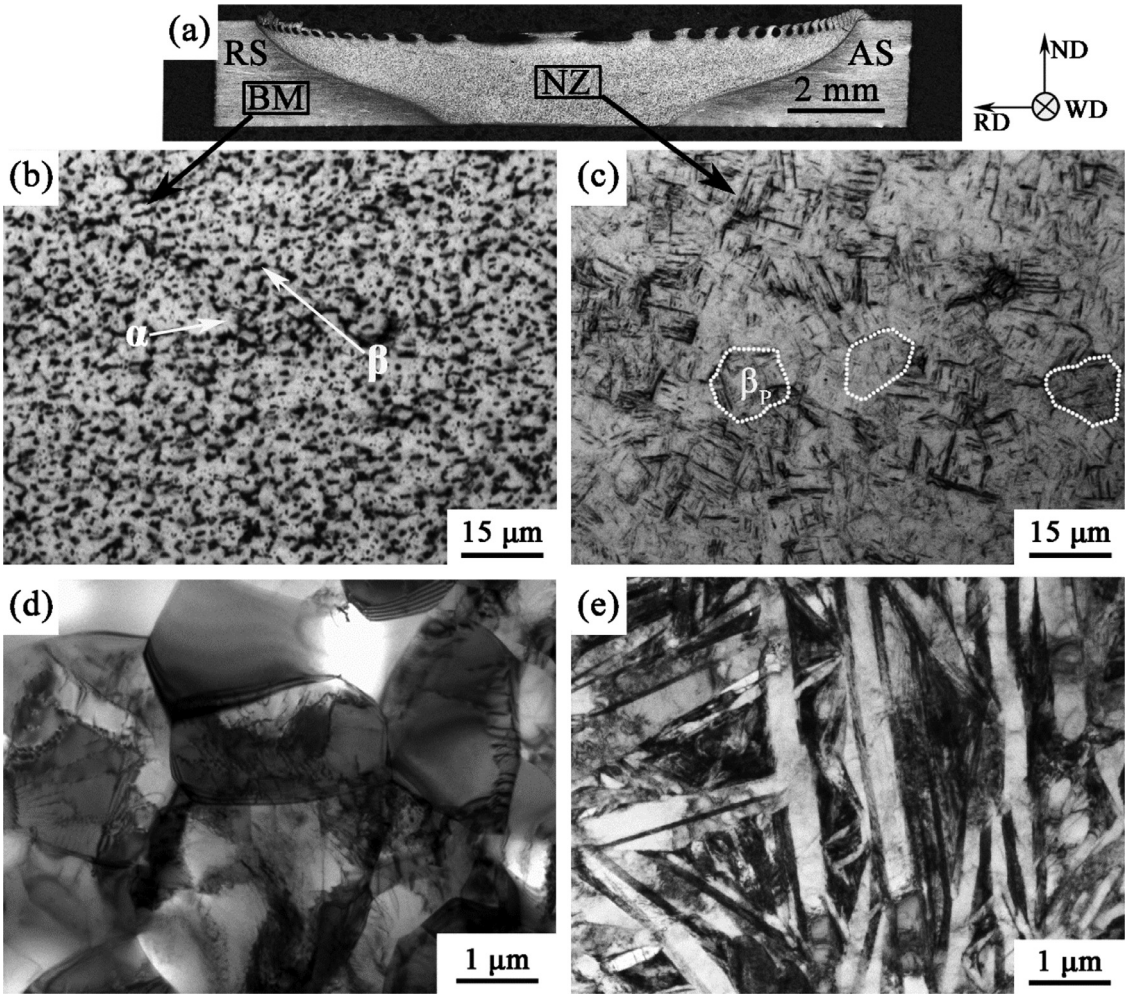


**Fig. 1..** OM images of (a) entire joint, (b) BM, and (c) NZ; TEM images of (d) BM, and (e) NZ.

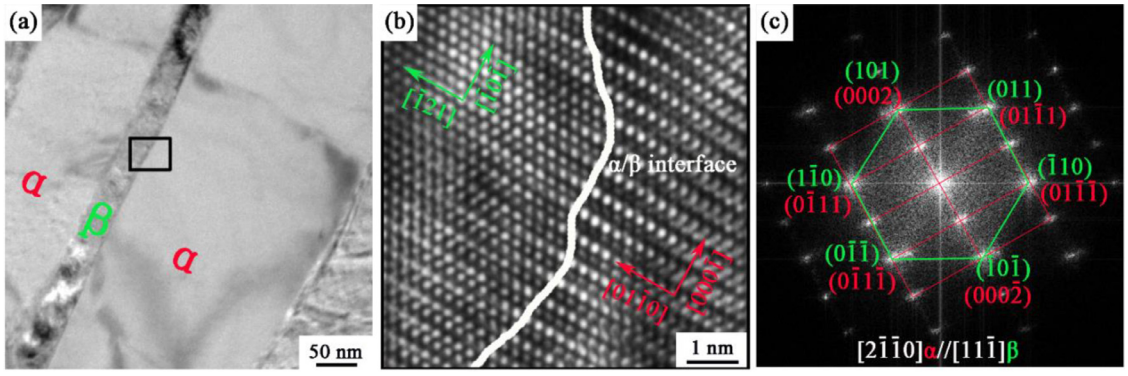


**Fig. 2.** Crystallographic characters of fully lamellar structure in NZ: (a) TEM bright field, (b) high-resolution TEM of $\alpha/\beta$ interface along $[2\bar{1}\bar{1}0]_\alpha$ // $[11\bar{1}]_\beta$ direction, (c) Fourier transformation taken from high-resolution TEM in $\alpha/\beta$ interface.

tween the lamellar $\alpha$ and $\beta$ phase after FSW [25], their actual orientation relationship was unclear, since there might be volume change or deformation even after the FSW tool passing away [26]. Thus, it is of great significance to verify the BOR of the lamellar structure especially in this study, due to its critical effect on the static spheroidization, which will be discussed in the following part .

The $\{10\bar{1}1\}$ twins are occasionally found in some acicular structures in the NZ (Fig. 3), indicating the unstable phase transformation after FSW, due to this type of twins usually occurring in the martensite under the high cooling rates [8].

### 3.2. Microstructural evolution of the BM and NZ during static annealing

Fig. 4 shows different morphologies in the BM and NZ at 900 °C under different annealing time. There was almost equiaxed $\alpha$ phase in the BM after annealing for 5 min (Fig. 4(a)). The grains of

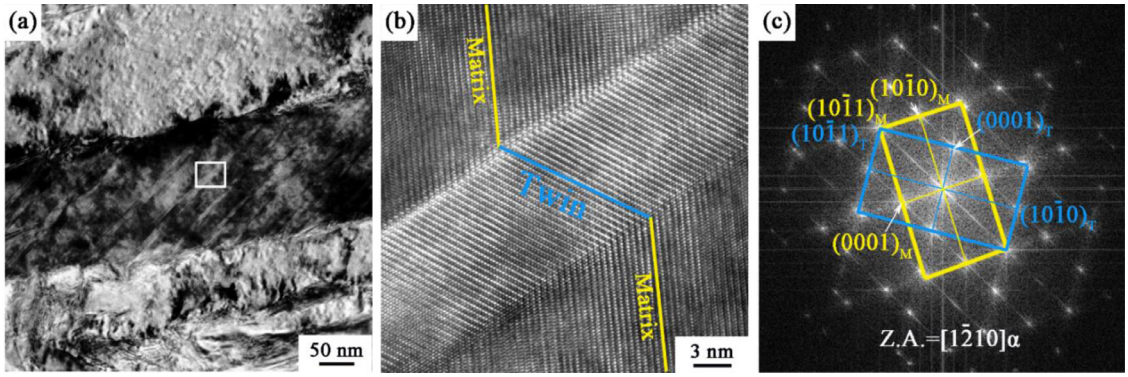


**Fig. 3.** Typical twins in NZ: (a) Bright field, (b) high-resolution TEM for selected area in (a) along [1$\bar{2}$10] direction, (c) Fourier transformation from high-resolution twin in (b).

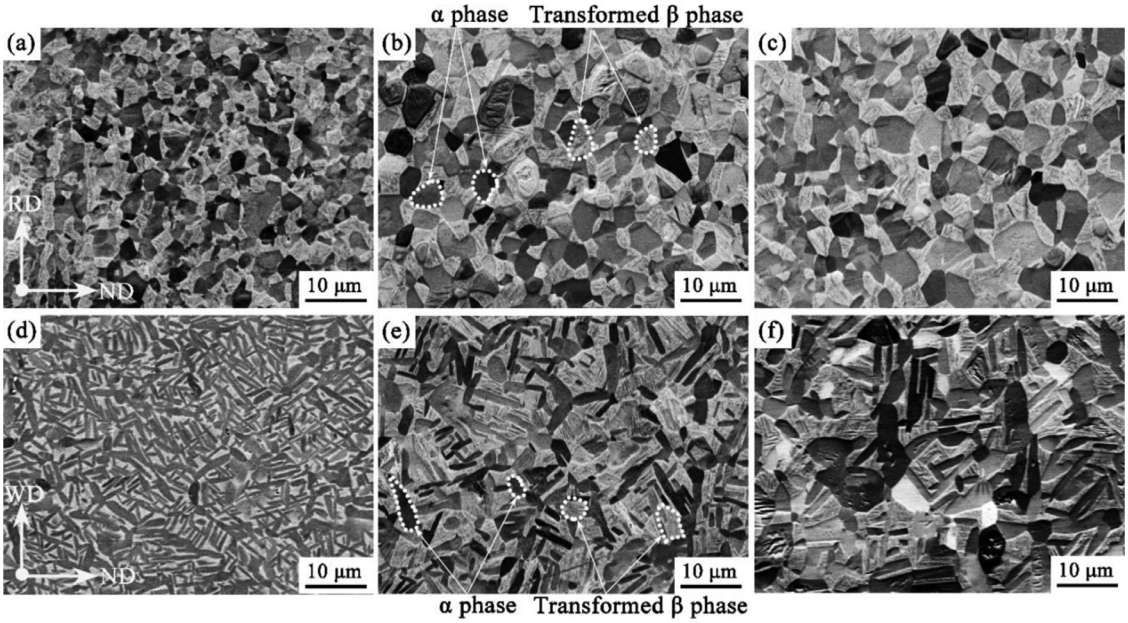


**Fig. 4.** Backscattered electron (BSE) images of BM and NZ after annealing at 900 °C for (a, d) 5 min, (b, e) 60 min, and (c, f) 180 min.

$\alpha$ phase were remarkably coarsened without loss of the equiaxed morphology (Fig. 4(a-c)), as the holding time increased. By contrast, some lamellae in the NZ were transformed into the equiaxed grains, as the annealing time increased (Fig. 4(d-f)), indicating an obvious static spheroidization behavior.

Figs. 5 and 6 present the EBSD band contrast (BC), All-Euler map and misorientation angle distribution for the BM and NZ after different annealing time. The volume fractions of $\alpha$ phase in the BM after annealing for 5, 60 and 180 min were 72.19%, 66.14%, and 60.83%, respectively, whereas, those in the NZ were 82.91%, 74.54%, and 73.62%, respectively, indicating a relatively higher volume fraction in the NZ than that in the BM. Fig. 5.(d–f) exhibits that the grains in the BM retained the initial equiaxed shape, but with a greater difference in the orientation, as the annealing time changed. There were some $\alpha$ phase colonies with the same color (marked in white dot lines) inside the NZ (Fig. 6(d–f)) at the beginning of static annealing. It inferred that the lamellae in $\alpha$ phase colonies were the same or similar orientations. The number of $\alpha$ phase colonies decreased largely at 900 °C for 180 min, where the mixed microstructure was formed consisting of the lamellar and equiaxed $\alpha$ phase (Fig. 6(f)). The equiaxed grains from the evolution of $\alpha$ colonies and the remaining lamellae in Fig. 6(f) showed a relatively large difference in the orientation from the surrounding microstructure. Consequently, the fine lamellar structure in the NZ can be spheroidized under static annealing without deformation.

Figs. 5(g–i) and 6(g–i) show some difference in the misorientation angle distribution for the BM and NZ. There was a relatively uniform distribution of misorientation angle that concentrated in the range of less than 10° in the BM (Fig. 5(g–i)). However, the misorientation angles are concentrated around 10°, 60° and 90° in the NZ (Fig. 6(g–i)), the peaks of which are more obvious than those of the BM after holding different time.

The misorientation angles can be concentrated around 10°, 60°, 63° and 90°, with the corresponding axis in <11$\bar{2}$0> and <0001>, if the $\alpha/\beta$ interface follows the BOR [25]. The special interface was eliminated by deformation during preparing the mill-annealed microstructure in the BM. The BOR presented in the lamellar structure of the NZ, as shown in Fig. 2.

However, the fine lamellar structure in the NZ after static annealing exhibited the spheroidization phenomenon without the assistance of the deformation, indicating a totally difference from the classical spheroidization theories [27].

The spheroidization rate of lamellar structure can also change with the increase of annealing time. Fig. 7(a–e) shows that the average aspect ratio of the lamellae decreased gradually, as the annealing time increased. Fig. 7(f) illustrates the spheroidization of

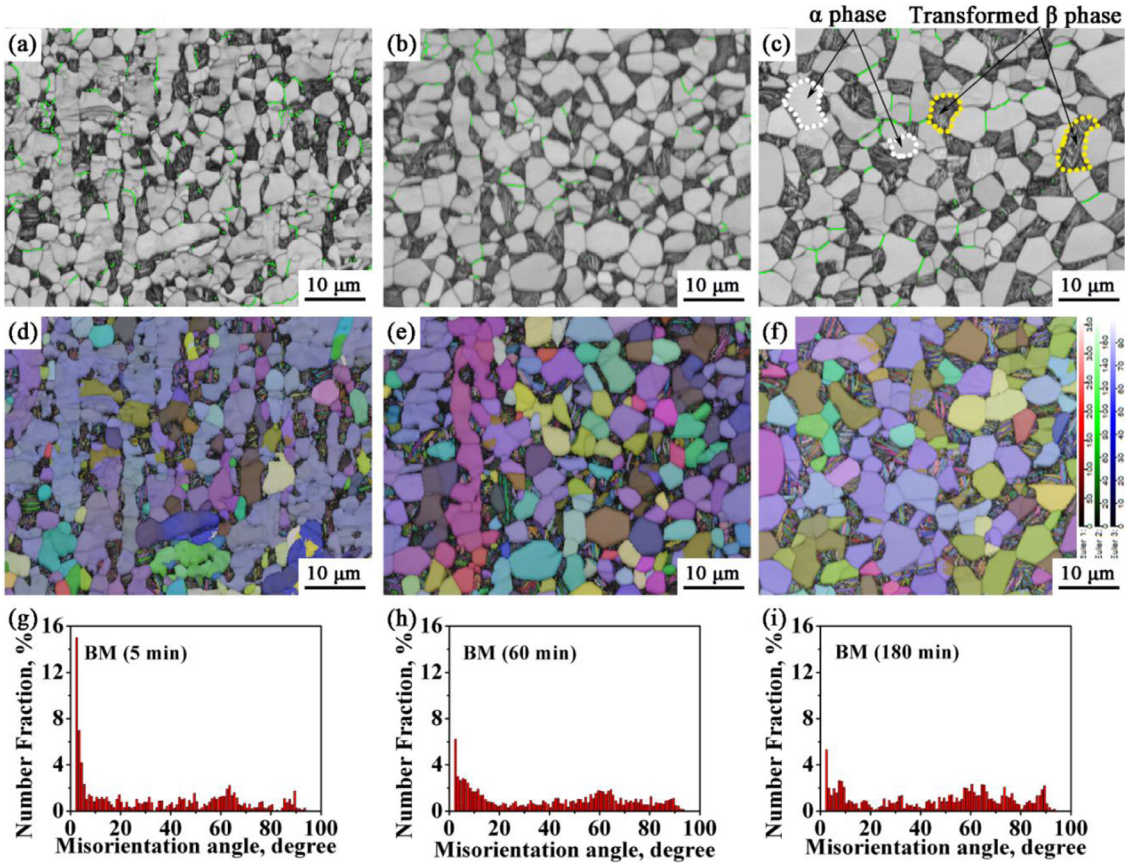


**Fig. 5.** EBSD BC/All-Euler map and misorientation angle distribution of BM after annealing at 900 °C for (a, d, g) 5 min, (b, e, h) 60 min, and (c, f, i) 180 min.

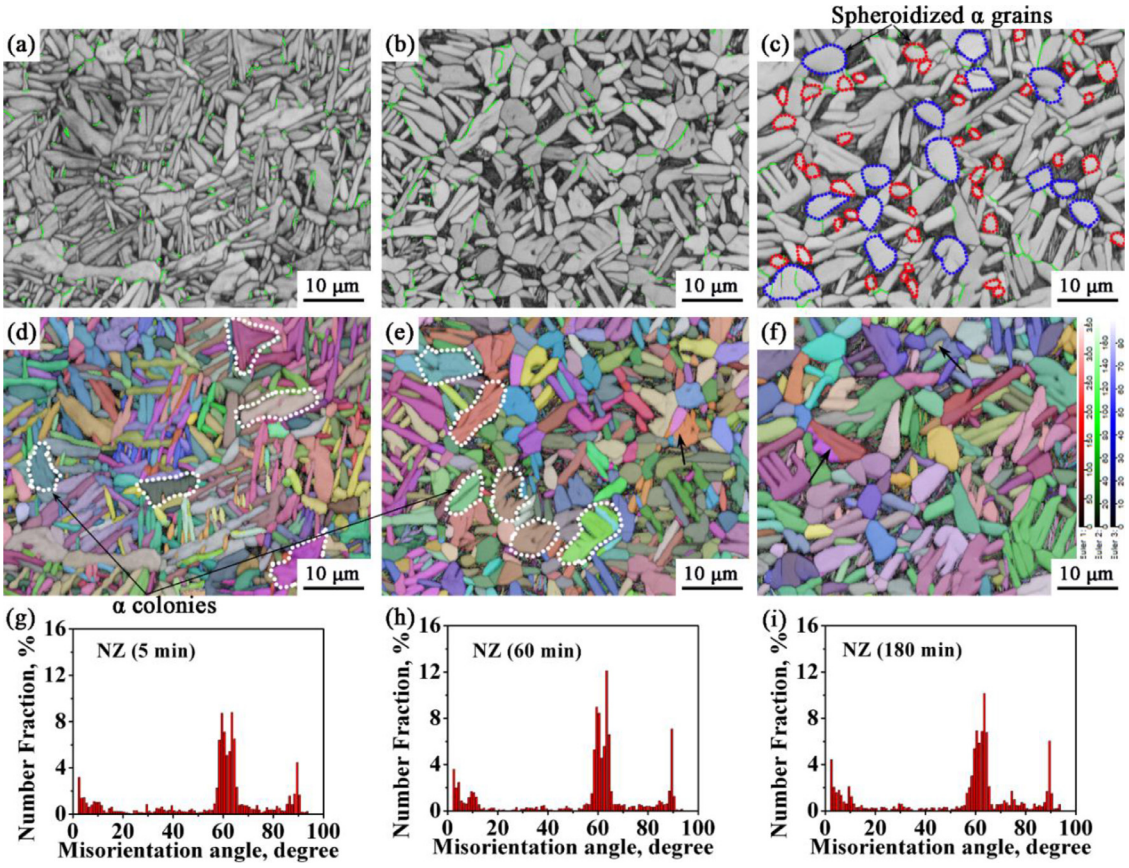


**Fig. 6.** EBSD BC/All-Euler map and misorientation angle distribution of NZ after annealing at 900 °C for (a, d, g) 5 min, (b, e, h) 60 min, and (c, f, i) 180 min.

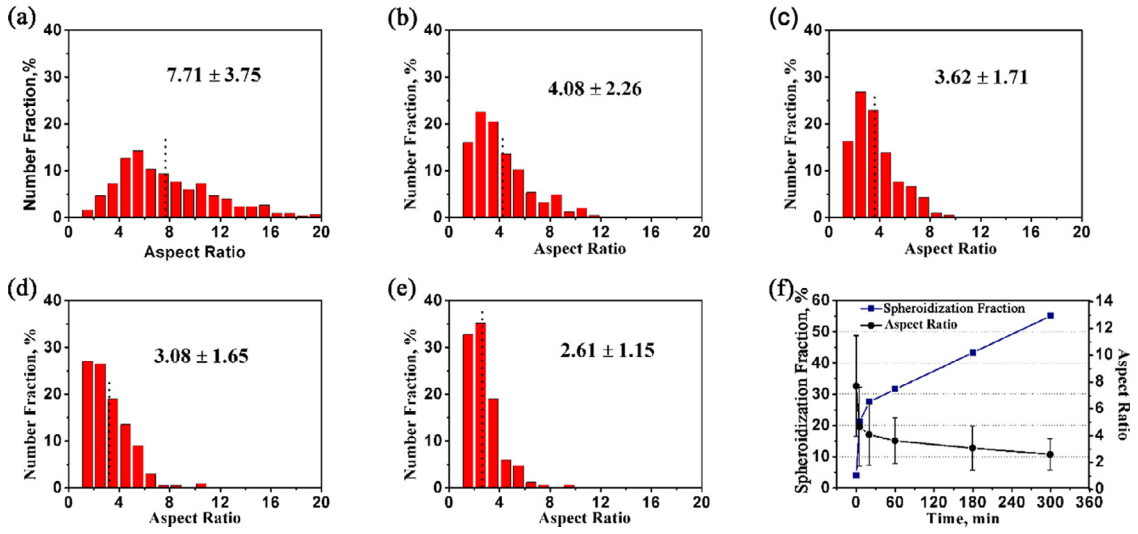


**Fig. 7.** Aspect ratio distribution of NZ after annealing for (a) 0 min, (b) 5 min (c) 60 min, (d) 180 min, (e) 300 min, and (f) spheroidization with annealing time.

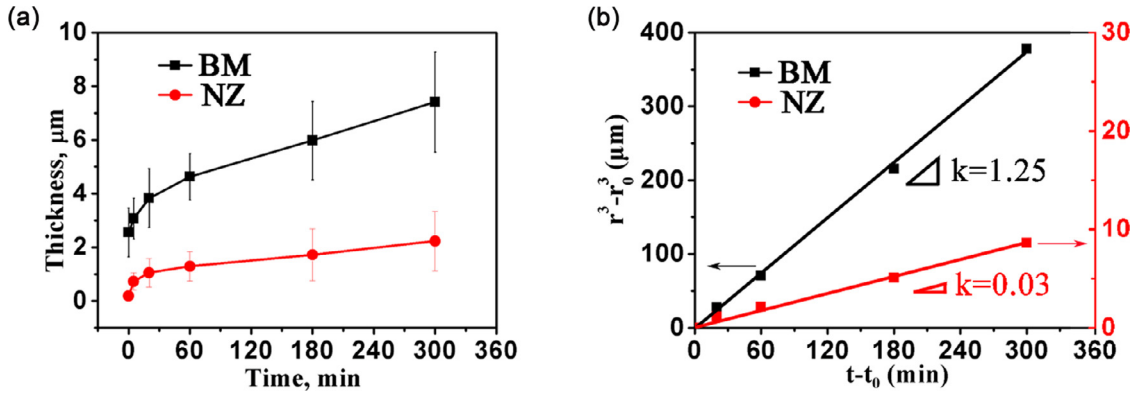


**Fig. 8.** (a) Thickness versus annealing time, and (b) coarsening behavior under static annealing, for BM and NZ.

lamellar $\alpha$ phase during annealing (the spheroidized grain is defined, when the aspect ratio is less than 2). In addition, a rapid spheroidization occurred in the early annealing stage, untill the spheroidization fraction reached over 25% at 20 min. Once the annealing time exceeded 60 min, the rate of spheroidization decreased significantly. The spheroidization fraction only increased to 55.1% after the heat preservation for 300 min at 900 °C. As such, the spheroidization of the lamellae can be divided into two stages according to the spheroidization rates and the holding time from 20 to 60 min could be defined as the dividing point (Fig. 7(f)).

### *3.3. Coarsening kinetics of equiaxed grains in the BM and the lamellae in the NZ*

A comparison was applied for the coarsening kinetic of the equiaxed structure and the lamellae, further to investigate the spheroidization behavior. As shown in Fig. 8(a), the coarsening rates of the equiaxed grains in the BM and the lamellae in the NZ both experienced an increasing trend first and then slowed down. However, the coarsening rate of the BM was higher than that of the NZ. Since the grain growth and morphology change generally follow the Ostwald ripening (OR) during annealing [28], the larger grains devour the smaller ones, as the annealing time increases. As such, the structure in the BM and NZ continued to coarsen, and the fluctuation of the thickness increased in Fig. 8(a), indicating the coarsening of the larger lamellae and the shrinking of the smaller ones. The fine grains marked by the red dotted lines in Fig. 6(c) also proved the shrinking of the small grains, as the time proceeded.

The LSW theory was widely accepted to describe the coarsening behavior [29]. Deriving from Gibbs–Thomson equation [30], the LSW theory described the grain growth and predicted the time-independent self-similar island-size distribution functions [31]. The relation of average grain radium $r$ with time $t$ is:

$$r^n - r_0^n = K(t - t_0) \tag{1}$$

where $r_0$ represents the average initial grain radius at the initial time $t_0$, $K$ is a temperature-dependent constant, $n$ is an exponent related to the coarsening. The kinetics is controlled by the interface reaction, when $n = 2$, while $n = 3$ by the volume diffusion. $r$ and $t$ represent the average grain radius and time, respectively.

The coarsening features of the BM and NZ related to the LSW theory are shown in Fig. 8(b). According to Eq. (1), the shape of curve gradually changes from the convex to concave, when $n$ changes from 1 to 4. The relation of $r^n - r_0^n$ and $t - t_0$ is close to be linear, when the value of $n$ is determined to be 3 for both the BM and NZ. Thus, the value of $K$ as the slope was a certain value. The best fit on $n = 3$ was close to be linear relationship for the equiaxed grains at 843 °C and 955 °C for the Ti-6Al-4V [17]. Here the coarsening of the lamellar structure was controlled by the volume diffusion, due to the lamellar structure with the linear ($n = 3$).

More importantly, there were different values of $K$ for the equiaxed grains and the lamellar structure. The static coarsening

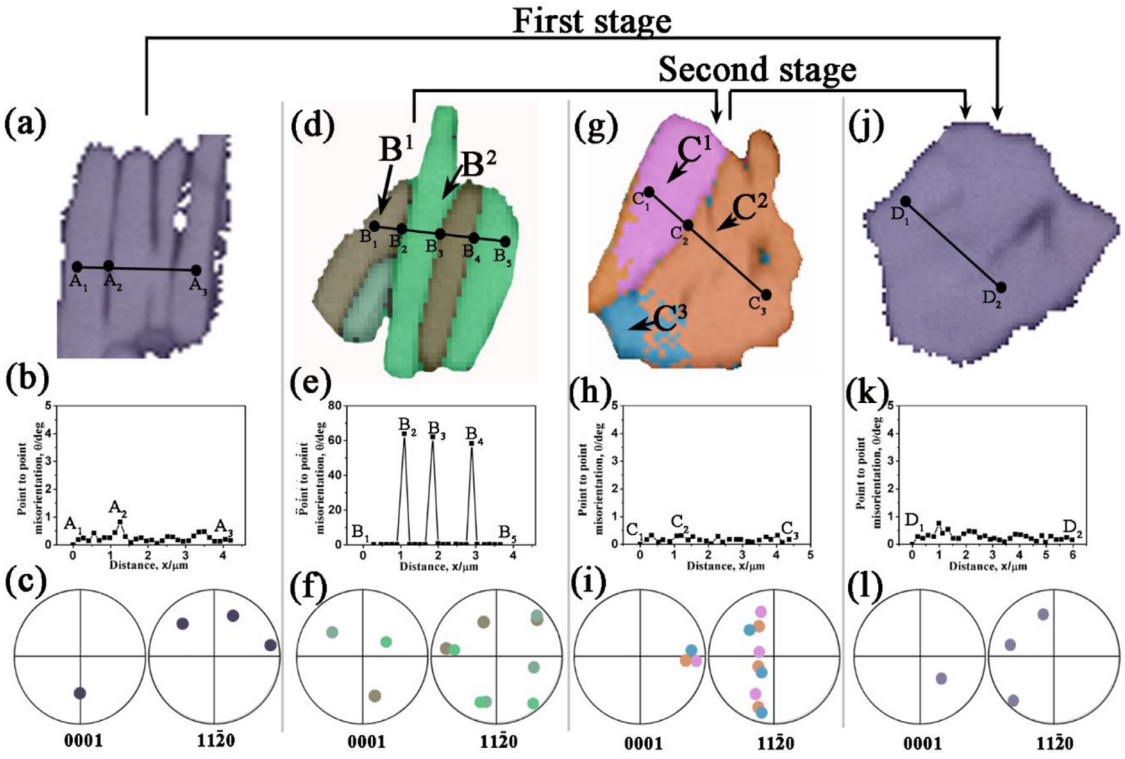


**Fig. 9.** (a, d, g, j) EBSD maps for typical lamellae under static annealing; (b, e, h, k) corresponding point to point misorientation along marked line, and (c, f, i, l) corresponding pole figure.

rates of equiaxed grains in the BM (75 $\mu m^3$/h) was about 42 times higher than those of the lamellae in the NZ (1.8 $\mu m^3$/h). In the classical LSW theory, the value of K is defined as follows:

$$K_{lsw}=\frac{8DG\gamma_{\alpha\beta}C_{\beta}V_M}{9RT} \quad (2)$$

where $D$ exhibits the diffusivity of the rate-limiting in the $\beta$ phase; $\gamma_{\alpha\beta}$ represents the $\alpha/\beta$ interface energy; $C_{\beta}$ is the equilibrium concentration of the rate-limiting solute in the $\beta$ phase; $V_M$ exhibits the molar volume of the $\alpha$; $T$ is the absolute temperature, and $R$ is the gas constant. The variables in Eq. (2) can pose a great influence on the value of $K$.

The coarsening rates depend mainly on the solutes in the materials with the lowest diffusivity under static annealing [32]. There was little difference in elements for the BM and NZ. Thus, the different coarsening rates for the BM and NZ can be attributed to the different $\alpha$ phase volume and the different $\gamma_{\alpha\beta}$ interface energy, according to Eq. (1).

The fraction of $\alpha$ phase in the NZ was higher than that in the BM (Figs. 5 and 6), indicating the normally higher coarsening rates for the NZ in theory.

However, the actual coarsening rates of lamellar structure in the NZ were much lower than those in the BM, indicating that the low-energy $\gamma_{\alpha\beta}$ for the lamellae greatly reduced the grain growth rates in the NZ.

### 3.4. Spheroidization mechanism of the lamellae during static annealing

Two types of lamellae in this study can be the $\alpha$ colonies with the same or similar orientation, and the lamellar structures with different orientations. As shown in Fig. 9(a), the point to point figure along the line $A_1A_3$ showed that the misorientation between the $\alpha$ colonies was less than 1.5° (Fig. 9(b)) after annealing for 5 min. The $\alpha$ colonies performed to be almost the same orientation in the pole figure in Fig. 9(c). Although there were the interfaces between the lamellae in the $\alpha$ colonies (Fig. 9(a)), the end of the lamellae began to merge into a complete grain with the interface disappearing. Nearly all the $\alpha$ colonies were coalesced to be a complete grain, after annealing for 60 min, as shown in Fig. 6(e). Pilchak and Williams [33] also found that there were the low-angle boundaries among lamellae for the $\alpha$ colonies in the NZ after FSW, accounting for about 17%. Therefore, the coalescence among the $\alpha$ colonies was one of the spheroidization in the NZ, where these adjacent lamellae with similar orientations can be the first step to be spheroidized.

There was a large fraction of lamellar structures with different orientations, such as the random oriented lamellae in Fig. 6(d). Fig. 9(d) demonstrates the obvious differences in Euler Angles between the lamellar structure $B^2$ and the surrounding ones. Fig. 9(e) shows that the misorientations exceed 60° at the point $B_2$ and $B_3$, although the adjacent lamellae share a similar orientation (Fig. 9(f)).

Fig. 9(g) shows the intermediate spheroidization for the lamellae with the different orientation. The different colors of the lamellar structure $C^1$, $C^2$ and $C^3$ represent for the different Euler angles among the adjacent structure. These lamellae with different orientation cannot be coalescent directly by the rotation of the whole structure, but by the rotation of part by part inside the lamellae. However, the point to point misorientation angles along line $C_1C_3$ were less than 1°, indicating almost the final stage of spheroidization, similar to the orientation of adjacent grains (Fig. 9(j)).

Fig. 9(j-l) shows the final state of the spheroidization process. The orientation difference between the lamellar structures was basically eliminated to form a complete equiaxed grain. Thus, the orientation difference between the adjacent lamellae was gradually reduced until disappeared via the gradual rotation of lamellae in Fig. 9(d, g, j), as the annealing time increased. As a re-

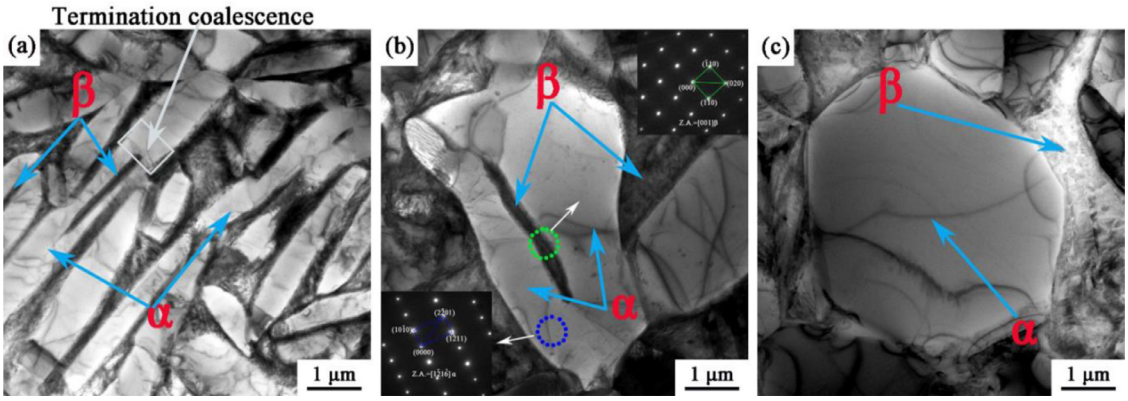


**Fig. 10.** TEM morphology of NZ after static annealing for the holding time of (a) 5 min, (b) 60 min, and (c) 300 min at 900 °C.

sult, the spheroidization was completed by the coalescence of the adjacent lamellae via the gradual rotation of the adjacent lamellae.

Although the coalescence with different orientations can occur during static annealing, the rotation among the adjacent lamellae can be more difficult, if there is too large orientation difference. Therefore, a large number of lamellar structures remained unspheroidized, even after annealing for 180 min at 900 °C (Fig. 6(c)). Furthermore, the presence of $\beta$ phase and the BOR can make the spheroidization more complex. Since the whole spheroidization was fully completed in the $\beta$-phase matrix, the coalescence firstly occurred at the end of lamellae, and the uncoalesced areas was filled with the $\beta$ phase (Fig. 10(a)). At the following step, the coalescence of lamellae was pushed to the middle part at the expense of the $\beta$ phase (Fig. 10(b)). Finally, the adjacent lamellae became a complete equiaxed grain (Fig. 10(c)).

Thus, the new static spheroidization mechanism in this study was different from the classical static spheroidization. In the classical termination migration, most dislocations can be accumulated inside the lamellar structure and the $\alpha/\beta$ interface during prestrain before static annealing, and thus the BOR in the $\alpha/\beta$ interface was partly broken [34]. As a result, the solute atoms can directly flow from the terminal to the middle of flat in the lamellae [20].

Here, the stable $\alpha/\beta$ interface prevented the further flow of solute atoms, indicating the very difficult migration of atoms from the termination into the middle of the lamellae [35], thus inducing the lower coarsening rates for the lamellae than those in the BM (Fig. 8(b)). As shown in Fig. 11(a), it was much easier for the atoms at the tip point $a_1$ (or $a_2$) migrated into the point $b_1$ (or $b_2$) than into the middle of the lamellae (point $c_1$ or $c_2$), due to the shorter distance and more chaotic atom arrangement at point $b_1$ (or $b_2$). In addition, the phase transformation more easily occurred, as the result of more active atom activities nearby the point b1 (or b2). All these processes resulted in the recession of the edges and the thickening in the lamellae (Fig. 11(b)).

Therefore, the ends of the lamellae with the same or similar orientation can be merged firstly to break the stability of the $\alpha/\beta$ interface, resulting in the increase in the disorder of atomic arrangement. The merged area can move gradually from both ends of the lamellae to the center along the $\alpha/\beta$ interface, driven by the interfacial curvature. At the center of lamellae, a rotation occurred in the center of adjacent lamellae as mentioned in Fig. 9, gradually leading to the similar orientation, even the same (Fig. 11(c)). Finally, a complete grain can be formed for the whole spheroidization (Fig. 11(d)). Here, we define this new spheroidization process as a “termination coalescence”, since this spheroidization mechanism has not been found before.

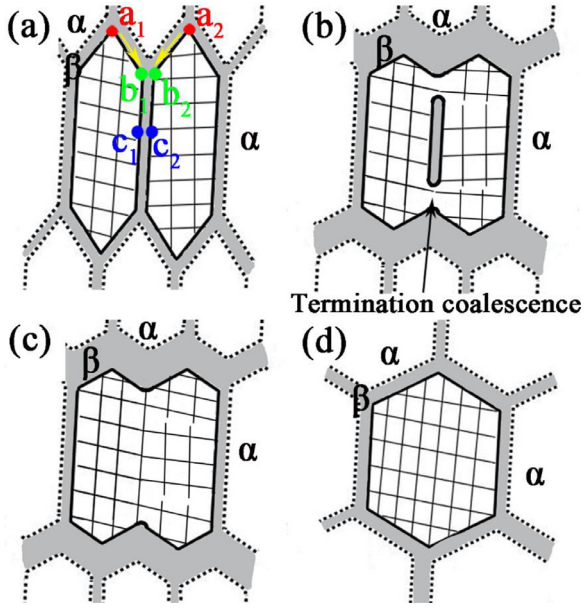


**Fig. 11.** Spheroidization mechanism of lamellae in NZ under static annealing: (a) initial state, (b) merging process of lamellar edges, (c) orientation of adjacent lamellae changing to be the same, (d) formation of a complete spheroidized grain.

Two stages can be divided in the entire spheroidization process of the fully lamellar structure in the NZ. The first stage underwent the fast spheroidization process. Fig. 9(a) shows the initial $\alpha$ colony with similar orientations.

Owing to the different diffusion and curvature among the tips and contracting point of adjacent lamellae, there are gradual contact and coalesce at the end of structure for the $\alpha$ colony. Meanwhile, the fine and low-aspect-ratio lamellae with the largely different orientation from the surroundings would go through the self-spheroidization process by the driving force of the curvature difference (the grains marked in red for Fig. 6(c)).

The second stage can be the slow spheroidization. The spheroidization rates gradually decreased, as the annealing time increased, as shown in Fig. 8(a). The spheroidization of $\alpha$ colonies with similar orientation have basically completed at this stage. The lamellar structure with a large difference in orientation gradually reduced the orientation difference to complete the spheroidization, as shown in Fig. 9(d-l). Meanwhile, there are some preserved lamellae with the obviously different orientation from the surroundings.

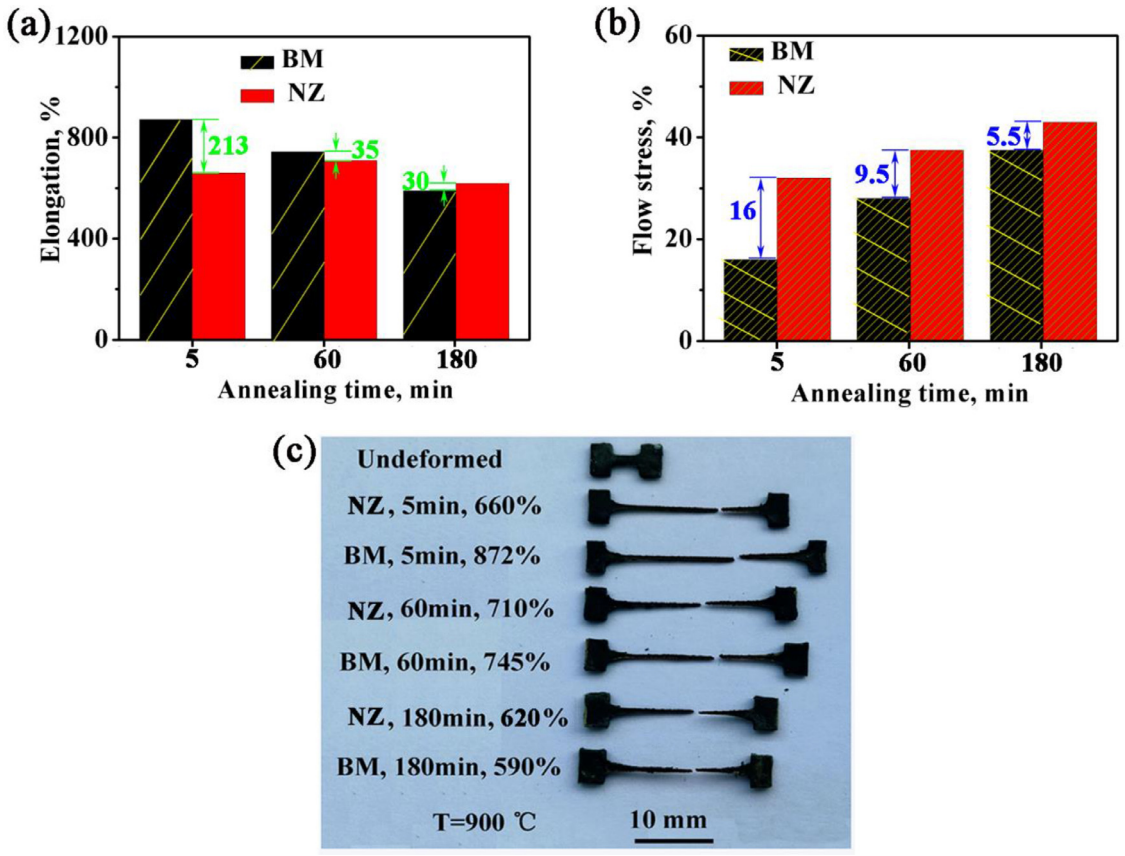


**Fig. 12.** Superplastic behavior of BM and NZ after annealing for different time: (a) elongation, (b) initial peak flow stress, and (c) macroscopic tensile specimens after fracture.

A similar rotation-coalescence of grains has been reported in the nanosize particles, especially during nanosintering [36]. The rotation process of grains can efficiently reduce the total grain boundary energy. However, only small grains can be rotated at high temperature (0.9 $T_m$, $T_m$ was the melting point), particularly the small orientation difference. The larger the grain size is, the higher the temperature is required for the coalescence [37]. In the coarser grains, the rotation of grains can occur only with the aid of applied stress [38]. Noted that the above description refers to the rotation of the whole grain. Since the temperature energy cannot drive the rotation of the whole grain, the whole lamellae were rotated part by part without the external stress in the study.

### 3.5. Effect of static annealing on the superplasticity of BM and NZ

The spheroidization and coarsening of lamellae (or grains) will finally affect the superplasticity of the BM and NZ during annealing. As shown in Fig. 12, the elongation of the NZ was much less than that of the BM, where the initial flow stress in the former was higher after annealing for 5 min . However, the difference of the elongation and initial peak flow stress between the BM and NZ reduced from more than 200% to 30%, and from 16 to 5.5 MPa, respectively, as the annealing time increased from 5 to 180 min. The tensile specimens indicated that the elongations exceeded 500% in the BM and NZ after annealing, with the uniform deformation in Fig. 12(c). Therefore, the superplastic abilities of the BM and NZ gradually trend to be similar after static annealing. Correspondingly, the similar superplasticity can be achieved in the BM and NZ by FSW + static annealing. The finding can provide a strong theoretical basis for the SPF of welded joints to fabricatethe large-scale components.

The reason with the similar superplasticity came from that there was the different influence of static annealing on the BM and NZ. In the BM, the static annealing can lead to the obvious coarsening for the equiaxed structure, thereby to decrease the elongation while increase the initial flow stress. However, the microstructure in the NZ exhibits a lower coarsening rate than that of the BM (Fig. 8), because the coarsening rate of the lamellar structure can be constrained by the low-energy $\alpha/\beta$ interface, as discussed in Section 3.3. Consequently, the superior stability can be obtained in the mixed equiaxed and lamellar structure than that in the fully equiaxed one at high temperature. Moreover, the inhomogeneous structure can obtain the excellent superplasticity [39].

Furthermore, by changing the proportion of the lamellar structure in the mixed structure by FSW, the yield strength and fatigue strength could be significantly changed. The mixed structure with a higher proportion of the lamellar structure exhibited a higher strength and fatigue property [40]. In this research, the proportion of the equiaxed structure in the mixed structure could be precisely controlled by controlling the static annealing time after obtaining the fully lamellar structure in the NZ. Consequently, the FSW process followed by static annealing can provided a new way to obtain an ideal mixed structure with the controlled fraction of the equiaxed and lamellar structure for a better mechanical property.

## 4. Conclusions

The FSW was utilized to obtain a fine lamellar structure with a low-aspect ratio in the NZ. An investigation was also made on the microstructure evolution and superplasticity of the BM and NZ under different annealing time. The following conclusions can be drawn.

(1) It is the first time to directly observe the BOR in the $\alpha/\beta$ interface for the transformed $\beta$ structure by FSW.
(2) The static coarsening rates of the equiaxed structure in the BM were about 42 times higher than that of the lamellae in the NZ. The trend was attributed to the constraint of low-energy $\alpha/\beta$ interface with the BOR in the lamellar structure. The static coarsening kinetics of lamellae was controlled by the bulk diffusion.
(3) The new spheroidization named as "termination coalescence" was found in the lamellae under static annealing, where the spheroidization process was first completed by the coalescence of the $\alpha$ colonies with the similar orientation, and then by the coalescence of lamellae with different orientation via the rotation part by part.
(4) The lamellar structure in the NZ can be changed into the mixed one with the increase of annealing time, whose superplastic ability was more stable than the classical equiaxed structure for the BM, resulting in the similar superplasticity for the BM and NZ.

## Acknowledgments

This work was supported by the National Natural Science Foundation of China (Nos. 51601194, 51471171, and U1760201), the Chinese Academy of Sciences Youth Innovation Promotion Association (No. 2021193), the Liaoning Provincial Natural Science Foundation (No. 2021-YQ-01), and the Liaoning Revitalization Talents Program (No. XLYC2002099).

## References

[1] Z.Q. Li, H.P. Guo, Mater. Sci. Forum 475-479 (2005) 3037–3042.
[2] R.R. Boyer, Mater. Sci. Eng. A 213 (1996) 103–114.
[3] C. Homer, J.P. Lechten, B. Baudelet, Metall. Trans. A 8 (1977) 1191–1193.
[4] S. Chen, J. Huang, D. Cheng, H. Zhang, X. Zhao, Mater. Sci. Eng. A 541 (2012) 110–119.
[5] C.G. Rhodes, M.W. Mahoney, W.H. Bingel, R.A. Spurling, C.C. Bampton, Scr. Mater. 36 (1997) 69–75.
[6] W. Zhang, H. Liu, H. Ding, H. Fujii, J. Alloy Compd. 803 (2019) 901–911.
[7] L.H. Wu, D. Wang, B.L. Xiao, Z.Y. Ma, Mater. Chem. Phys. 146 (2014) 512–522.
[8] L.H. Wu, X.B. Hu, X.X. Zhang, Y.Z. Li, Z.Y. Ma, X.L. Ma, B.L. Xiao, Acta Mater. 166 (2019) 371–385.
[9] S. Mironov, Y.S. Sato, H. Kokawa, J. Mater. Sci. Technol. 34 (2018) 58–72.
[10] F.C. Liu, Y. Hovanski, M.P. Miles, C.D. Sorensen, T.W. Nelson, J. Mater. Sci. Technol. 34 (2018) 39–57.
[11] P. Edwards, M. Ramulu, D.G. Sanders, Key Eng. Mater. 433 (2010) 169–176.
[12] L.H. Wu, D. Wang, B.L. Xiao, Z.Y. Ma, Scr. Mater. 78-79 (2014) 17–20.
[13] L.H. Wu, B.L. Xiao, D.R. Ni, Z.Y. Ma, X.H. Li, M.J. Fu, Y.S. Zeng, Scr. Mater. 98 (2015) 44–47.
[14] W. Zhang, H. Liu, H. Ding, H. Fujii, Mater. Sci. Eng. A 785 (2020) 139390.
[15] X. Gao, W. Zeng, Y. Wang, Y. Long, S. Zhang, Q. Wang, J. Alloy Compd. 725 (2017) 536–543.
[16] S.L. Semiatin, M.W. Corbett, P.N. Fagin, G.A. Salishchev, C.S. Lee, Metall. Mater. Trans. A 37A (2006) 1125–1136.
[17] S.L. Semiatin, B.C. Kirby, G.A. Salishchev, Metall. Mater. Trans. A 35A (2004) 2809–2819.
[18] S. Zherebtsov, M. Murzinova, G. Salishchev, S.L. Semiatin, Acta Mater. 59 (2011) 4138–4150.
[19] E.B. Shell, S.L. Semiatin, Metall. Mater. Trans. A 30 (1999) 3219–3229.
[20] J. Xu, W. Zeng, H. Ma, D. Zhou, J. Alloy Compd. 736 (2018) 99–107.
[21] Z.B. Zhao, Z. Liu, Q.J. Wang, J.R. Liu, R. Yang, J. Mater. Sci. Technol. 35 (2019) 591–595.
[22] S.L. Semiatin, N. Stefansson, R.D. Doherty, Metall. Mater. Trans. A 36A (2005) 1372–1376.
[23] L.H. Wu, P. Xue, B.L. Xiao, Z.Y. Ma, Scr. Mater. 122 (2016) 26–30.
[24] X. Zheng, S. Zheng, J. Wang, Y. Ma, H. Wang, Y. Zhou, X. Shao, B. Zhang, J. Lei, R. Yang, X. Ma, Acta Mater. 181 (2019) 479–490.
[25] S. Mironov, Y. Zhang, Y.S. Sato, H. Kokawa, Scr. Mater. 59 (2008) 511–514.
[26] A.L. Pilchak, W. Tang, H. Sahiner, A.P. Reynolds, J.C. Williams, Metall. Mater. Trans. A 42 (2010) 745–762.
[27] N. Stefansson, S.L. Semiatin, Metall. Mater. Trans. A 34 (2003) 691–698.
[28] J. Zhang, F. Huang, Z. Lin, Nanoscale 2 (2010) 18–34.
[29] I.M. Lifshitz, V.V. Slyozov, J. Phys. Chem. Solids 19 (1961) 35–50.
[30] A.J. Ardell, Acta Metall. 20 (1972) 601–609.
[31] M. Iwamatsu, Y. Okabe, J. Appl. Phys. 86 (1999) 5541–5548.
[32] C.H. Park, B. Lee, S.L. Semiatin, C.S. Lee, Mater. Sci. Eng. A 527 (2010) 5203–5211.
[33] A.L. Pilchak, J.C. Williams, Metall. Mater. Trans. A 42A (2011) 773–794.
[34] M. Cabibbo, S. Zherebtsov, S. Mironov, G. Salishchev, J. Mater. Sci. 48 (2012) 1100–1110.
[35] S. Balachandran, A. Kashiwar, A. Choudhury, D. Banerjee, R. Shi, Y. Wang, Acta Mater. 106 (2016) 374–387.
[36] Z.Z. Fang, H. Wang, Int. Mater. Rev. 53 (2008) 326–352.
[37] A.J. Haslam, S.R. Phillpot, H. Wolf, D. Moldovan, H. Gleiter, Mater. Sci. Eng. A 318 (2001) 293–312.
[38] B. Ratzker, A. Wagner, M. Sokol, S. Kalabukhov, N. Frage, Acta Mater. 164 (2019) 390–399.
[39] Y. Zhang, S. Chang, Y. Chen, Y. Bai, C. Zhao, X. Wang, J.M. Xue, H. Wang, J. Mater. Sci. Technol. 95 (2021) 225–236.
[40] A.L. Pilchak, J.C. Williams, Metall. Mater. Trans. A 42 (2010) 1630–1645.